

Article

Boosting the Photoelectrochemical Water Oxidation Performance of TiO₂ Nanotubes by Surface Modification Using Silver Phosphate

Prabhakarn Arunachalam ^{1,*}, Mabrook S. Amer ^{1,2,*}, Haneen A. AlOraij ¹, Abdullah M. Al-Mayouf ^{1,2}, Mahmoud Hezam ^{3,4} and Matar Al-Shalwi ¹

¹ Electrochemical Sciences Research Chair, Department of Chemistry, Science College, King Saud University, Riyadh 11451, Saudi Arabia

² K.A.CARE Energy Research and Innovation Center at Riyadh, Riyadh 11451, Saudi Arabia

³ King Abdullah Institute for Nanotechnology, King Saud University, Riyadh 11451, Saudi Arabia

⁴ Physics Department, College of Science, Imam Mohammad Ibn Saud Islamic University (IMSIU), Riyadh 13318, Saudi Arabia

* Correspondence: parunachalam@ksu.edu.sa (P.A.); msamer@ksu.edu.sa (M.S.A.); Tel.: +966-114696026 (P.A.)

Abstract: Photoelectrocatalytic approaches are fascinating options for long-lasting energy storage through the transformation of solar energy into electrical energy or hydrogen fuel. Herein, we report a facile method of fabricating a composite electrode of well-aligned TiO₂ nanotubes (TNTs) decorated with photodeposited silver phosphate (Ag₃PO₄) nanoparticles. Assessment of the optical, physiochemical and photoelectrochemical features demonstrated that the fabricated TNTs/Ag₃PO₄ films showed a substantially boosted photocurrent response of 0.74 mA/cm², almost a 3-fold enrichment in comparison with the pure TNTs. Specifically, the applied bias photon-to-current efficiency of the fabricated TNTs/Ag₃PO₄ composite electrode was 2.4-fold superior to that of the pure TNTs electrode. In these TNTs/Ag₃PO₄ photoanodes, the introduction of Ag₃PO₄ over TNTs enhanced light absorption and improved charge transfer and surface conductivity. The developed process can be generally applied to designing and developing efficient contact interfaces between photoanodes and numerous cocatalysts.

Keywords: photoelectrochemistry; TiO₂ nanotubes; silver phosphate; water oxidation



Citation: Arunachalam, P.; Amer, M.S.; AlOraij, H.A.; Al-Mayouf, A.M.; Hezam, M.; Al-Shalwi, M. Boosting the Photoelectrochemical Water Oxidation Performance of TiO₂ Nanotubes by Surface Modification Using Silver Phosphate. *Catalysts* **2022**, *12*, 1440. <https://doi.org/10.3390/catal12111440>

Academic Editors: Yongpeng Liu and Yong Zuo

Received: 15 September 2022

Accepted: 10 November 2022

Published: 15 November 2022

Publisher's Note: MDPI stays neutral with regard to jurisdictional claims in published maps and institutional affiliations.



Copyright: © 2022 by the authors. Licensee MDPI, Basel, Switzerland. This article is an open access article distributed under the terms and conditions of the Creative Commons Attribution (CC BY) license (<https://creativecommons.org/licenses/by/4.0/>).

1. Introduction

The exploitation of the solar-assisted photoelectrochemical (PEC) method to yield H₂ clean fuel through water oxidation is significant, as it involves cost-effective semiconductors and is driven by renewable solar energy [1,2]. Selecting the proper electrode for the PEC process is mandatory, as the electrode must absorb visible-light photons and yield photoinduced charge carriers, which can be applied economically for industrial uses [3,4]. To powerfully transform solar photons into chemical fuels, semiconducting materials with acceptable band energy levels and low overpotentials are required, as they can arrest a larger region of the solar spectrum to execute the hydrogen and/or oxygen evolution reaction (HER/OER). In recent years, tremendous research work has been performed to endorse competitive n-type semiconductor candidates as photocatalysts, since the OER is a kinetically more complicated process, and therefore suffers from severe oxidizing circumstances. In order to realize this, different kinds of metal oxide-based photoanode materials have been widely explored (e.g., TiO₂ [5], ZnO [6], SrTiO₃ [7], Fe₂O₃ [8], and WO₃ [9,10]). More importantly, TiO₂ is recognized as an appropriate electrode material for the photoelectrochemical water-splitting scheme to generate hydrogen, due to its acceptable energy level position, high optical as well as chemical stability, and chemical inertness [11–13]. Although the wider bandgap (~3.2 eV) of bare TiO₂ limits its usage and

limits its optical absorption to the UV portion of the spectrum, resulting, besides the slow carrier transport, in lower electrochemical features [14], TiO₂ nanotubes (TNTs) provide a direct path to photocarriers with a high catalytic surface area. Since TNTs were explored by Hoyer via a template-aided method [15], the effect of the fabrication characteristics, doping strategies, and uses of TNTs have been widely explored [16–18]. In this context, highly oriented TNTs have been demonstrated in the literature to be excellent electrode candidates, owing to their greater durability, great efficiency under UV light, sustainable features, and tendency to possess abundant potential for wide absorption with reduced recombination [19–21]. To achieve superior efficiency, the sensitization of TiO₂ materials has been carried out by narrow-bandgap materials [22,23], and metal nanoparticles [24] are frequently created. However, it is still a huge task to fabricate highly effective TNTs photoanodes with appropriate water oxidation co-catalysts (WOC) in order to decrease the driving force of the water-splitting systems.

Recently, incorporating n-type semiconductor materials with a WOC has been found to be a suitable route for boosting the photoelectrochemical features of TNT films, as well as reducing the recombination rate of photoinduced charge carriers [25]. For instance, incorporating transition metal phosphides/phosphates has been explored as a way to boost the water-splitting systems [26–29]. Specifically, one of the most favorable candidates demonstrated so far has been silver phosphate, Ag₃PO₄, an indirect bandgap semiconductor with a bandgap of 2.45 eV that is capable of capturing solar photons of up to 500 nm in the visible-light region [30–32]. Interestingly, significant recent efforts have been carried out to decorate Ag nanoparticles over the Ag₃PO₄ surface, which acted as an electron acceptor, improving the charge separation and inhibiting the deterioration of Ag₃PO₄. Inspired by these earlier reports, we have reported on BiVO₄-based electrodes loaded with nanostructured Ag₃PO₄ for the water oxidation reaction [32]. Interestingly, we also established that having both oxygen vacancies in the bulk and metal doping over the surface of the TNT array films can efficiently increase the efficiency of the light-driven water oxidation reaction [33–35]. Therefore, the synergistic combination of TNTs with Ag₃PO₄ decoration can be an effective approach to improving light-driven water oxidation reactions.

Herein, a series of silver-phosphate-decorated TNT electrodes were obtained through the chemical photodeposition process, and their photoelectrochemical features in water-splitting reactions are explored. The fabricated TNTs/Ag₃PO₄ electrodes exhibited a superior photocurrent density (0.74 mA/cm² at +1.23 V_{RHE}), signifying almost a 3-time enrichment over its parent TNTs. We attribute the boosted PEC features to the narrower band-gap of the composite electrode and the reduced charge recombination resulting from the combination of plasmonic Ag nanoparticles over the TNTs surface.

2. Results and Discussion

2.1. Crystalline Properties of TNTs/Ag₃PO₄ Arrays

The overall procedure to decorate Ag₃PO₄ nanoparticles over TNTs films is defined in Figure S1 (Supplementary Materials). With this chemical photodeposition method and voltammetric scans, good regulation over the number of Ag₃PO₄ deposited layers over the TNTs surfaces were acquired. The initial optimization of the photodeposition concentrations of Ag nanoparticles was performed using numerous varied concentrations (0.01–0.2 M [AgNO₃]). The optimal Ag concentration in the TNTs for effective electrodes was observed to be 0.05 M.

A crystalline analysis was performed to inspect the role of Ag₃PO₄ incorporation over the fabricated TNTs in the photoelectrochemical performances. Initially, an X-ray diffraction (XRD) analysis of TNTs, TNTs/Ag, and TNTs/Ag₃PO₄ photoelectrode materials was performed (Figure 1a). Interestingly, the acquired diffraction patterns for all the electrodes were observed at 25.1°, 46.5°, and 54.6°, which are the diffraction patterns corresponding to the (1 0 1), (2 0 0), and (2 1 1) diffraction planes of the pure anatase TiO₂ phase (JCPDS 21-1272) [36]. No other peaks related to Ag or Ag₃PO₄ were noticed in the relevant XRD patterns, reflecting the small loading of the co-catalyst. The average

crystallite sizes of the bare TNTs, Ag/TNTs, and Ag₃PO₄/TNTs were calculated to be 22 nm, 30, and 34 nm, respectively, as evaluated by the Scherrer formula [37]. These values can, however, be unreliable, as the Scherrer formula considerably diverges for anisotropic tubular shapes with high aspect ratios like TNTs [38,39].

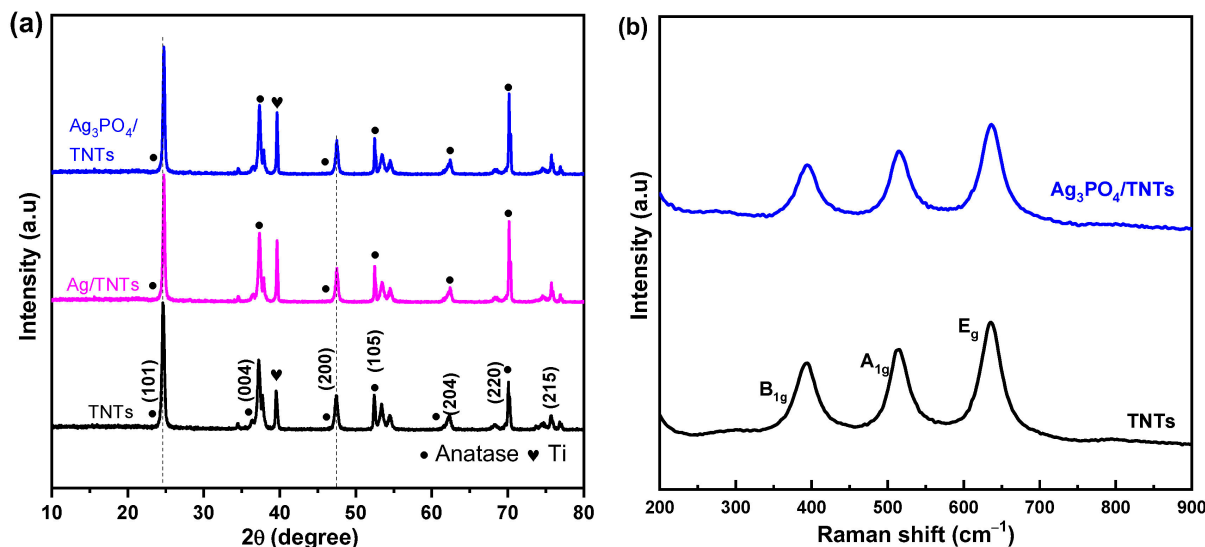


Figure 1. Crystalline features of electrodes (a) X-ray diffraction patterns of bare TNTs (black), optimized TNTs/Ag electrodes (magenta) obtained by photodeposition process, and TNTs/Ag₃PO₄ (blue) electrodes obtained through photodeposition process (b) Raman spectra of pure TNTs (black), TNTs/Ag₃PO₄ electrodes.

Further, Raman spectroscopy has been applied as a sensitive system to observe the phase and surface composition of the fabricated electrodes. The Raman spectroscopic characterization of pure TNTs and TNTs/Ag₃PO₄ electrodes is presented in Figure 1b. It is clearly evidenced that the anatase phase dominates the crystal structure of the pure and Ag₃PO₄-loaded electrodes. Anatase has six Raman-active vibrational modes ($1A_{1g} + 2B_{1g} + 3E_g$) [40]. The B_{1g} , A_{1g} , and E_g reflections, respectively, at 392 cm^{-1} , 513 cm^{-1} , and 636 cm^{-1} all confirm the anatase phase of the TNTs. After Ag₃PO₄ decoration over the TNTs, no signal related to Ag or Ag₃PO₄ nanoparticles was identified, perhaps because of the fairly low concentration of Ag incorporation onto the TNTs and its weak Raman scattering. This validated that Ag nanoparticles decoration does not considerably affect the crystalline features of TNTs electrode films.

2.2. Optical Properties of TNTs/Ag₃PO₄ Arrays

Diffuse reflectance spectroscopy (DRS) was engaged to explore the optical properties of the unmodified TNTs, TNTs/Ag, and TNTs/Ag₃PO₄ array films; the acquired spectra are presented in Figure 2a,b. The optical analysis presented in Figure 2a clearly validates that Ag₃PO₄ incorporation boosts the optical absorption features of TNTs between 380 and 800 nm. Mostly, the TNTs array surface absorbs the light photons in the UV region. Interestingly, the UV-Vis analysis evidenced that the Ag₃PO₄ incorporation improved the light absorption intensity in the visible region. The shift of absorption towards the visible region can also be partially attributed to the plasmonic response of the Ag particles decorated over the TNTs electrodes. In order to evaluate the effective band gaps of pure and composite electrodes, which is a mandatory step for identifying the effectiveness of decorating with Ag₃PO₄ when used as an electrode co-catalyst, Tauc plots were generated and are shown in Figure 2b. From these plots, the effective band gap is estimated to be 3.18 and 2.83 eV for the TNTs and TNTs/Ag₃PO₄ electrode materials, respectively. The bandgap for the pure TNT array film is in agreement with earlier described reports [41]. The Ag₃PO₄ layer modified the effective bandgap of the TNT electrode. In addition, absorption

in the visible range can also be observed, and it extends from just above the band edge at ~ 400 nm to the end of the visible spectrum. Previous reports have demonstrated that Ag/Ag₃PO₄ nanostructures induce light scattering [42], which enhances the overall light absorption process.

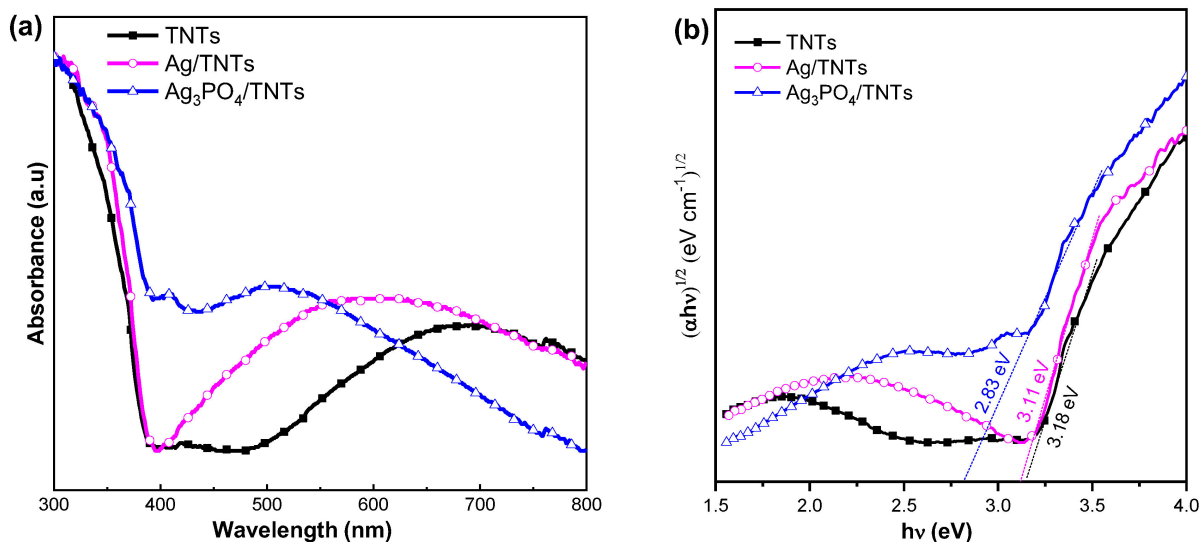


Figure 2. Optical features of electrodes. (a) Normalized UV-Vis absorbance spectra and (b) its corresponding Tauc plot relationship among $(\alpha h\nu)^{0.5}$ and E (eV) for fabricated TNTs films and Ag nanoparticles decorated TNTs, and TNTs/Ag₃PO₄, with bandgaps of 3.18, 3.11 and 2.83 eV, respectively.

2.3. Surface Features of TNTs/Ag₃PO₄ Arrays

Figure 3 displays the surface morphological properties of the TNTs/Ag₃PO₄ array films as observed by Field Emission Scanning Electron Microscopy (FE-SEM). The Ag₃PO₄ decorated TNTs (Figure 3a,b) preserved their open-top structure and incessant nanotubular morphology, maintaining an accessible surface area for the diffusion of electrolyte ions. As shown in Figure 3a,b, morphological examination reveals a well-ordered, vertically aligned tubular structure, with a nanotube diameter in the range between ~ 95 to 115 nm, a nanotube length of about ~ 550 nm, and a wall thickness of ~ 18 nm. No obvious accumulation of Ag₃PO₄ has been witnessed over the TNTs surface. Also, minor fragments of cracks exist within the nanotube walls. Figure 3c shows cross-sectional images of the TNTs/Ag₃PO₄ composite film. Again, the TNTs were well-aligned, and the tube diameters and wall thicknesses did not vary with Ag₃PO₄ decoration. Energy dispersive x-ray spectroscopy (EDS) examination determined the Ag doping levels in the obtained films. Figure 3d displays the EDS spectrum; Ag, P, Ti, and O peaks are evident, revealing the incorporation of the Ag₃PO₄ layer.

The formation of a well-organized interface between TNTs and Ag₃PO₄ was assessed by High-Resolution Transmission Electron Microscopy (HRTEM) analysis. Figure 4a,b illustrates the HRTEM photographs of the TNTs/Ag₃PO₄ electrodes, which confirm the homogeneity and arrangement of the obtained NTs arrays. Moreover, the developed TNTs displayed an outer diameter of 170 ± 2 nm and a wall thickness of 20 ± 2 nm. The high-resolution HRTEM photograph (Figure 4c,d) demonstrates distinctive lattice fringes of 0.352 nm, which agrees with the (101) diffraction plane of anatase TiO₂ (JCPDS no. 21-1272). Remarkably, the TNTs/Ag₃PO₄ array electrodes were distinguished by the existence of 5–10 nm nanocrystallites on the TNTs surface (Figure 4d).

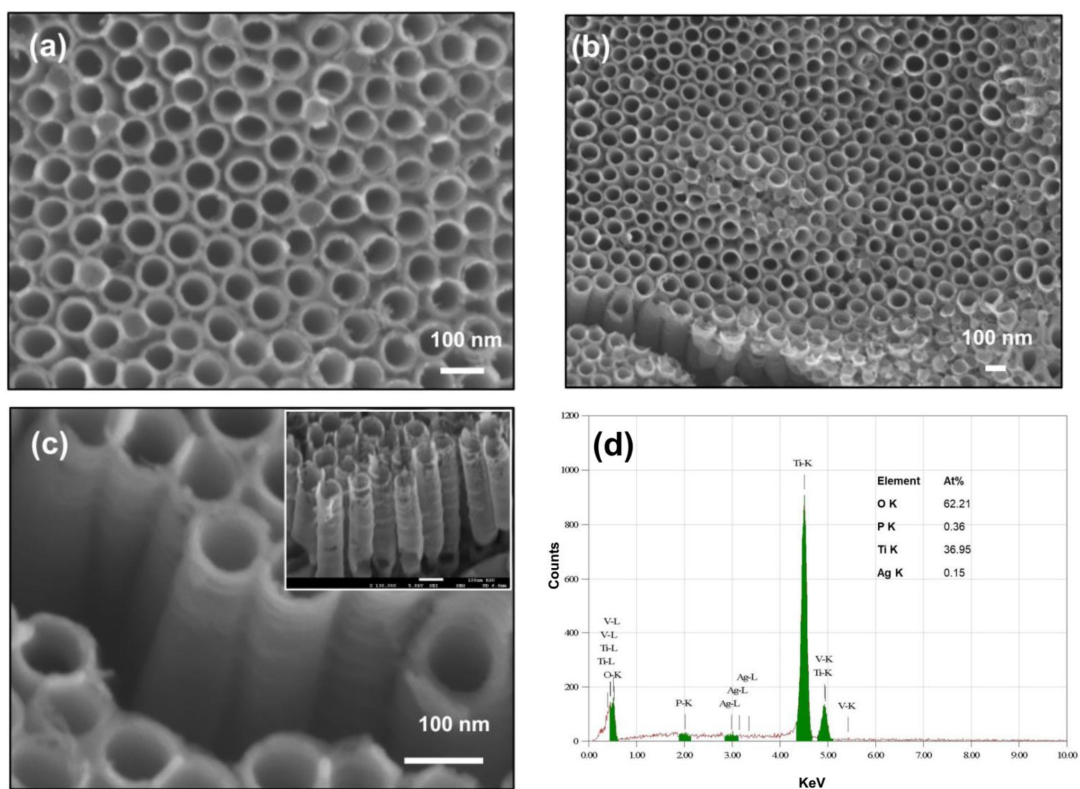


Figure 3. Morphological features of electrodes. (a,b) FE-SEM top-view images of Ag_3PO_4 photodeposited over TNTs substrate and (c) its cross-sectional view showing the TNTs walls of TNTs/ Ag_3PO_4 film. (d) EDS results for TNTs/ Ag_3PO_4 electrodes.

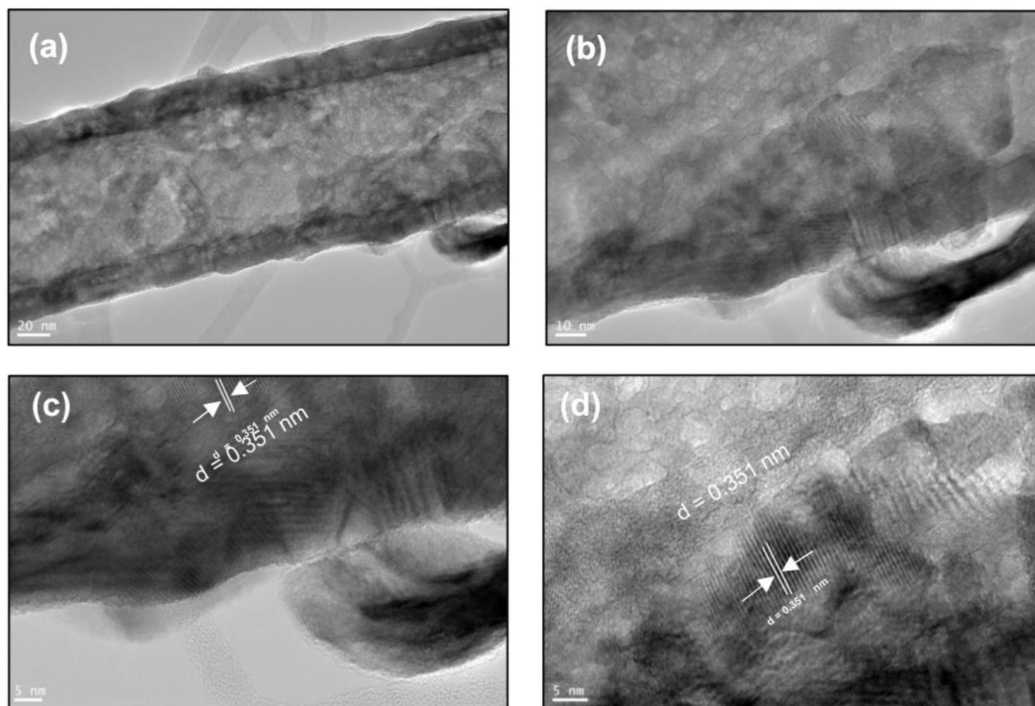


Figure 4. (a,b) HR-TEM images of the TNTs/ Ag_3PO_4 array films prepared using a two-step anodization process; (c,d) at a higher magnification of TNTs/ Ag_3PO_4 .

The chemical state of each component in the TNTs/Ag₃PO₄ array films was examined by X-ray Photoelectron Spectroscopy (XPS). Figure 5a demonstrates the XPS survey scan of both pure and TNTs/Ag₃PO₄ composite electrodes, in which the peaks of Ti, O, Ag, and P could all be observed. The high-resolution Ti 2p spectra of both electrodes are displayed in Figure 5b. The two main peaks, located at 464.0 and 459.2 eV, agree to Ti 2p_{1/2} and 2p_{3/2}, respectively, which specifies the 4+ state of Ti allied with TNTs. Further, the peak-to-peak positions and 5.86 eV peak separation of the Ti 2p doublet agree well with TiO₂ [43]. Figure 5c illustrates the O 1s spectra of the TNTs and TNTs/Ag₃PO₄ electrodes. The O 1s spectra evidence the prominent peak at ~530.4 eV and another shoulder peak at 531.5 eV, revealing the presence of two different O chemical states in the prepared electrodes [44]. The asymmetry of the Ag 3d peaks suggests the existence of dissimilar oxidation states for Ag on the TNTs/Ag₃PO₄ film electrodes. After deconvolution, two main peaks at 374.1 and 367.9 eV are resolved (Figure 5d), corresponding with the Ag 3d_{3/2} and Ag 3d_{5/2} orbitals of Ag⁺, respectively [45]. In addition, the smaller shoulder peaks at 374.2 and 368.2 eV are characteristic of the metallic Ag⁰ oxidation state. The presence of metallic Ag over the surface of Ag₃PO₄ is reported to function as an electron acceptor to boost the photoinduced charge carrier separation and inhibit the reductive breakdown of Ag₃PO₄ [46]. Also, the P 2p peak representing P⁵⁺ in the phosphate group can be recognized at 133.4 eV in the TNTs/Ag₃PO₄ composite films, as seen in Figure 5e, validating the development of the Ag₃PO₄ phase.

The O 1s, Ti 2p_{3/2}, Ag 3d_{5/2}, and P 2p_{3/2} peaks were applied to quantify the chemical composition of the surface of the composite electrode. The atomic percentages of oxygen, Ti, Ag, and P were calculated to be respectively 62.1%, 29.1%, 1.2%, and 7.6%. When compared to the EDX compositional analysis (inset in Figure 3d), the differences are informative about the film homogeneity of the Ag₃PO₄ layer. First, the increase in the at% of both Ag and P is consistent with the surface sensitivity of the XPS technique. XPS is a surface technique that probes only the top 2–3 nm of the sample, while EDX microanalysis can go deeper into the sample. However, the Ti at% of 29.1% (compared to 36.95% in EDX) detected by XPS is still substantial, indicating the ultra-small thickness of the Ag₃PO₄ layer over the TNTs surface.

2.4. Photoelectrochemical Performances of TNTs/Ag₃PO₄ Arrays

The photoelectrochemical performance of the fabricated TNTs, and of the TNTs/Ag and TNTs/Ag₃PO₄ array films best optimized toward PEC water splitting, was explored under continuous/chopped visible-light photons in a 0.1 M PBS solution. Figure 6a displays the linear sweep voltammogram (LSV) plots at 10 mVs⁻¹ while in-situ light pulsing for TNTs/Ag₃PO₄ composite array films decorated with an upsurging quantity of Ag nanoparticles deposited in PBS solutions. Remarkably, the acquired photocurrent response rises from 0.25 to 0.9 mA/cm² as the concentration of AgNO₃ increases from 0 to 0.2 M, owed to improved light absorption and, thus, enhanced photoinduced carrier density. The maximal photocurrent response of 0.9 mA/cm² was attained at a concentration of 0.05 M and 1.23 V_{RHE} (Figure 6b). At higher concentrations of Ag (>0.05 M), the photogenerated holes need to be transported between numerous Ag₃PO₄ crystallites to reach Ag₃PO₄/electrolyte interface sites, which substantially decreases the kinetics of the hole transfer process, and, therefore, a lesser current density is witnessed [47]. Figure 6c illustrates the LSV plots of the fabricated TNTs and TNTs/Ag₃PO₄ array films at 5 mV/s. Under illumination, an acquired photocurrent at 1.23 V_{RHE} was demonstrated on the order of TNTs/Ag₃PO₄ (0.74 mA/cm²), which is a 3-fold enrichment compared to the unmodified TNTs films TNTs (0.24 mA/cm²). The onset potential was also reduced with Ag₃PO₄ decoration. Under the chopped condition, as seen in Figure 6d, the optimal TNTs/Ag₃PO₄ electrodes also revealed boosted photocurrent response compared to the unmodified TNTs. The estimated photocurrent response can be attributed to the enhanced oxygen evolution reaction [48], which is greater upon Ag₃PO₄ introduction over TNTs films. This considerable decline in onset potential and enhancement in photocurrent density demonstrate a superior water splitting reaction, which may be enhanced by the

higher absorption (and so higher carrier density), efficient photoinduced carrier separation, and reduced rate of electron-hole recombination. Figure 6e illustrates the curves of the applied bias photon-to-current efficiency (ABPE) with respect to potential. Specifically, the pure TNTs array films show an optimum ABPE efficiency of 0.253%. Remarkably, the TNTs/Ag₃PO₄ composite film showed higher efficiency, with a maximum ABPE of 0.58% at a relatively lower bias of ~0.33 V_{RHE}. Therefore, nearly 2-fold enhancement in ABPE efficiency at a reduced applied bias resulted from the decoration of Ag₃PO₄ on the TNTs. Lastly, the photoinduced charge carrier separation and charge transport within Ag₃PO₄ can be other major aspects behind the improved PEC features of TNTs/Ag₃PO₄ composite films.

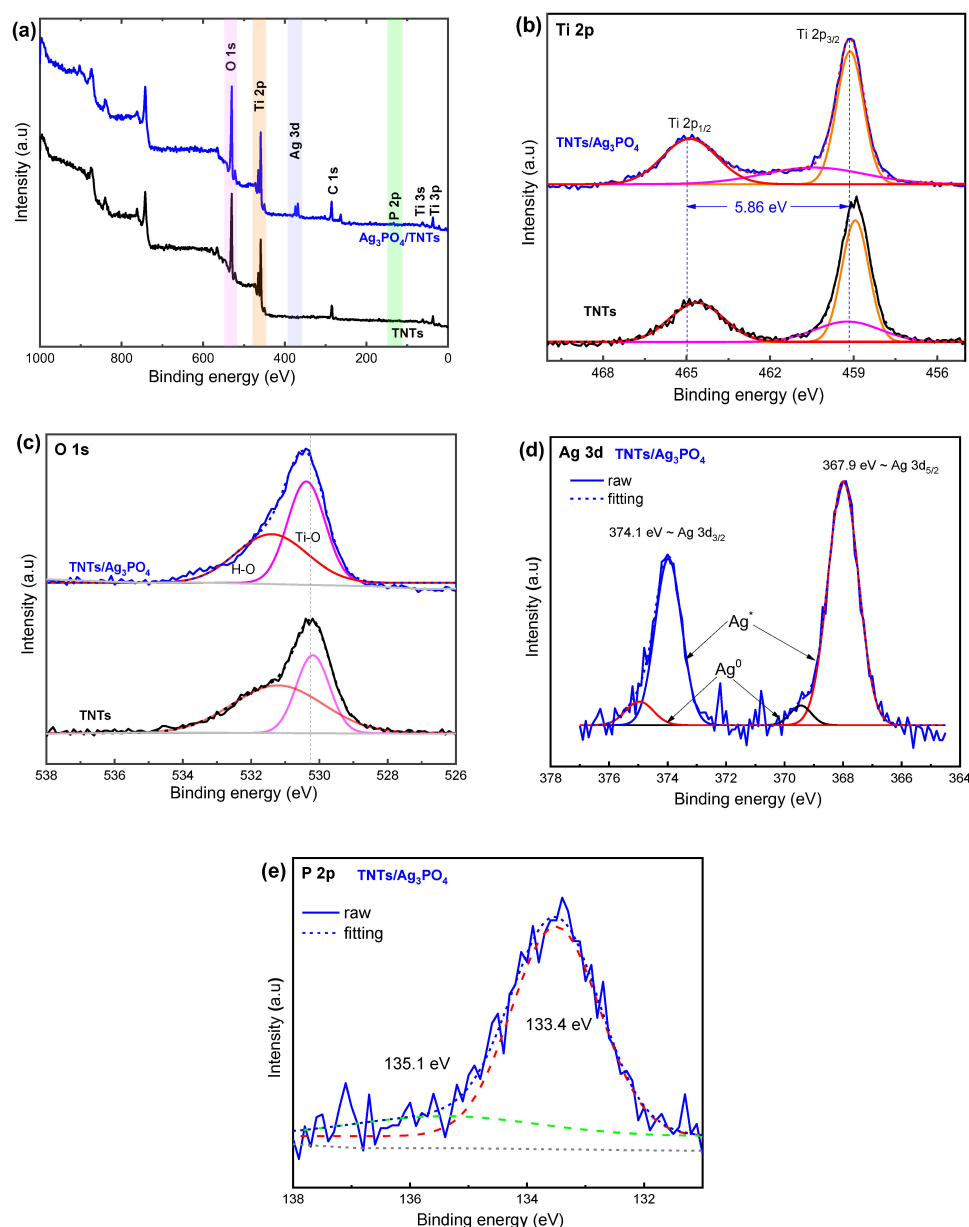


Figure 5. Surface features of electrodes. XPS-survey spectrum of TNTs (black), and TNTs/Ag₃PO₄ (blue) (a), and the High-resolution Ti 2p spectra (b), O 1s spectra (c), Ag 3d spectra (d), and P 2p (e) spectra of TNTs, and TNTs/Ag₃PO₄ array films. The solid line is fitted; the dashed line is the experimental line.

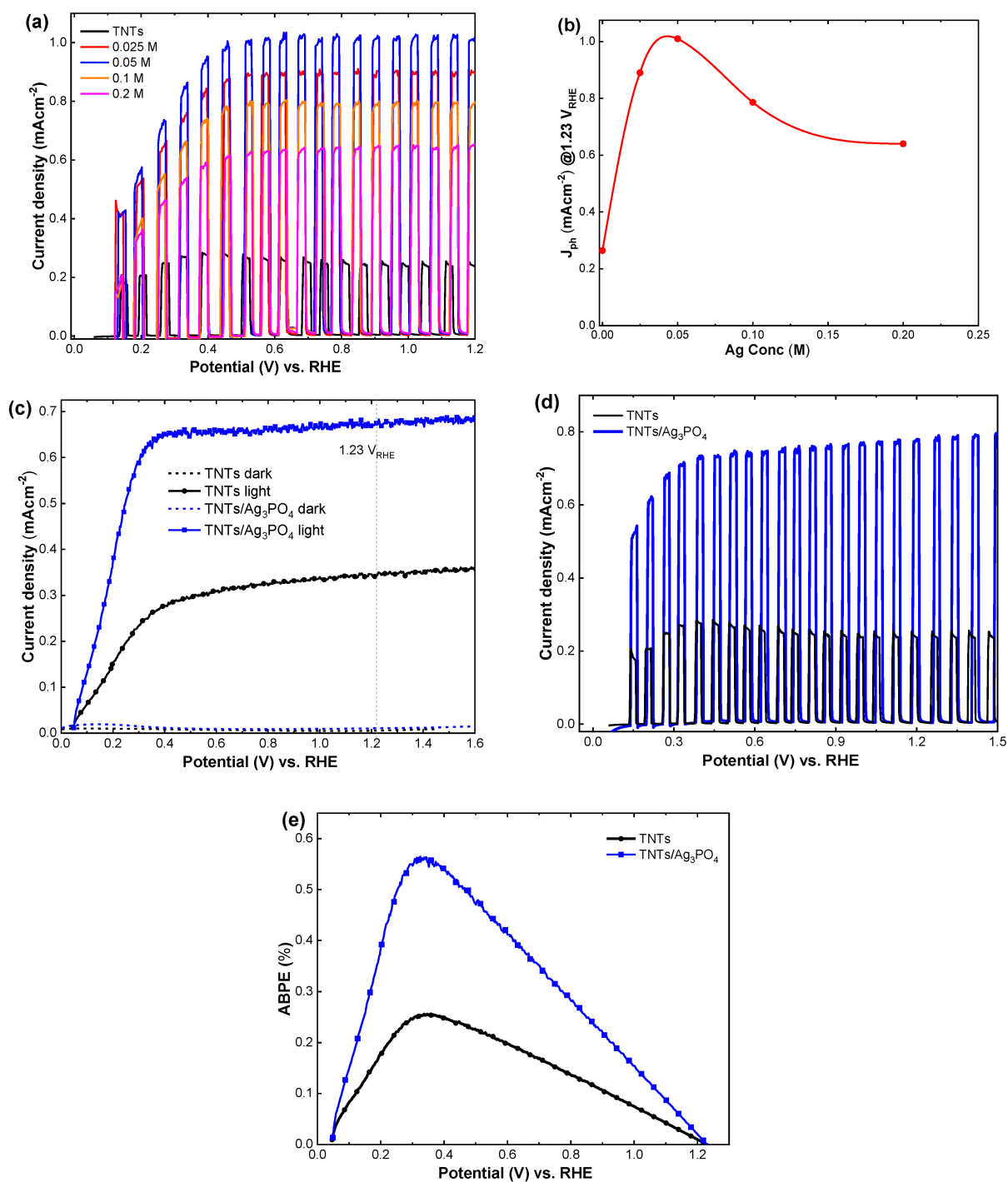


Figure 6. (a) Transient photocurrents obtained for TNTs array films with varied Ag nanoparticles using chemical photodeposition process; (b) Photocurrent response acquired at 1.23 V_{RHE} by varying the Ag concentration in the chemical photodeposition process. (c) Linear sweep voltammetric (LSV) curves of fabricated TNTs, optimized TNTs/Ag electrodes, and TNTs/Ag₃PO₄ acquired under constant irradiations (1.5 G AM); (d) corresponding LSV plots attained for TNTs films and TNTs/Ag₃PO₄ array films under chopped irradiation; (e) estimated photoconversion efficiencies plots received for TNTs arrays, TNTs/Ag and TNTs/Ag₃PO₄ electrodes.

Further data to explicate the origin of the improved PEC features of the TNTs/Ag₃PO₄ array films were obtained from a voltammetry analysis with the presence of a Na₂SO₃ sacrificial hole scavenger, as seen in Figure 7a. In addition, the Figure 7b curves show the photocurrent response of the TNTs/Ag₃PO₄ array films with and without Na₂SO₃. It is evident that the TNTs/Ag₃PO₄ films displayed an obvious enrichment of the photocurrent response and a reduction of onset potential in the presence of Na₂SO₃. The hole scavenger reduces the recombination of charge carriers and improves the injection of photoinduced holes into the electrolyte. Surface charge transfer (η_{surface}) efficiency was accordingly calculated for the fabricated TNTs and TNTs/Ag₃PO₄ films at different applied biases, using Equation (2). It has been confirmed that 100% of the photoinduced holes are exploited in Na₂SO₃ oxidation, which means η_{surface} is 100% [49]. Indeed, the TNTs array films produced only <35% η_{surface} , even at a higher applied bias, at which the greater electric field hampers surface carrier recombination. Notably, after decorating with Ag₃PO₄, η_{surface} of the TNTs/Ag₃PO₄ composite array films was enhanced to ~84% at 1.23 V_{RHE}, signifying enhanced charge transfer kinetics. This can be understood by reference to the TNTs/Ag₃PO₄ type II heterojunction structure (Figure 7f), which improves the charge carrier separation. In addition, it was reported that Ag₃PO₄ can also enhance the stability of the nanotubes by decreasing the recombination of charge carriers via the rapid and comprehensive OER [32].

The stability/durability test was performed on the optimized TNTs/Ag₃PO₄ photoanodes, using chronoamperometric measurements at 1.23 V_{RHE} evaluated in PBS (0.1 M, pH 7.5), under constant illumination conditions (Figure 7d). The chronoamperometric plots for the TNTs/Ag₃PO₄ electrode showed improved stability compared to the pure TNT electrode; subsequently, after 8 h of chronoamperometric tests, 62.50% of its early performances were sustained (0.42 vs. 0.74 mA/cm²). Table S1 (Supplementary Materials) compares the photocatalysts fabricated in the present study with those in earlier reports. Moreover, to evaluate the mass loss through the durability test, an XRD and FE-SEM of the TNT/Ag₃PO₄ composite film were attained at eight hours. Notably, the obtained TNTs/Ag₃PO₄-treated film had no obvious modifications in its diffraction pattern (Figure 7e) and FESEM images (Figure S2, Supplementary Materials) after 8 h, compared to the fresh electrode.

The interfacial charge transfer features were examined by electrochemical impedance spectroscopy (EIS), as seen in Figure 8a. The Nyquist plots of the TNTs/Ag₃PO₄ and the TNTs array films assessed under illumination conditions at 1.0 V_{RHE}, along with the equivalent circuit, are presented in Figure 8a. Interestingly, under illumination, the diameter of the arc radius is much lesser for the TNTs/Ag₃PO₄ array films than for the pure TNTs, revealing fast interfacial charge transfer through the interface, and an effective separation of photoinduced electron-hole pairs, resulting in greater PEC properties [50]. The choice of the equivalent electrical circuit is dependent on the behavior of the plots, as seen from the inset of Figure 8a; two-time constants were seen, and the fitted curves were in good agreement with the experimental data throughout the entire frequency range. As reported previously [51,52], the most appropriate circuit for the analysis of TNTs is (Rs(Q1(R1(Q2R2))))). Evidently, Ag₃PO₄-addition enriched the charge-carrier density and electronic conductivity, thereby decreasing the resistance (Table S2, Supplementary Materials).

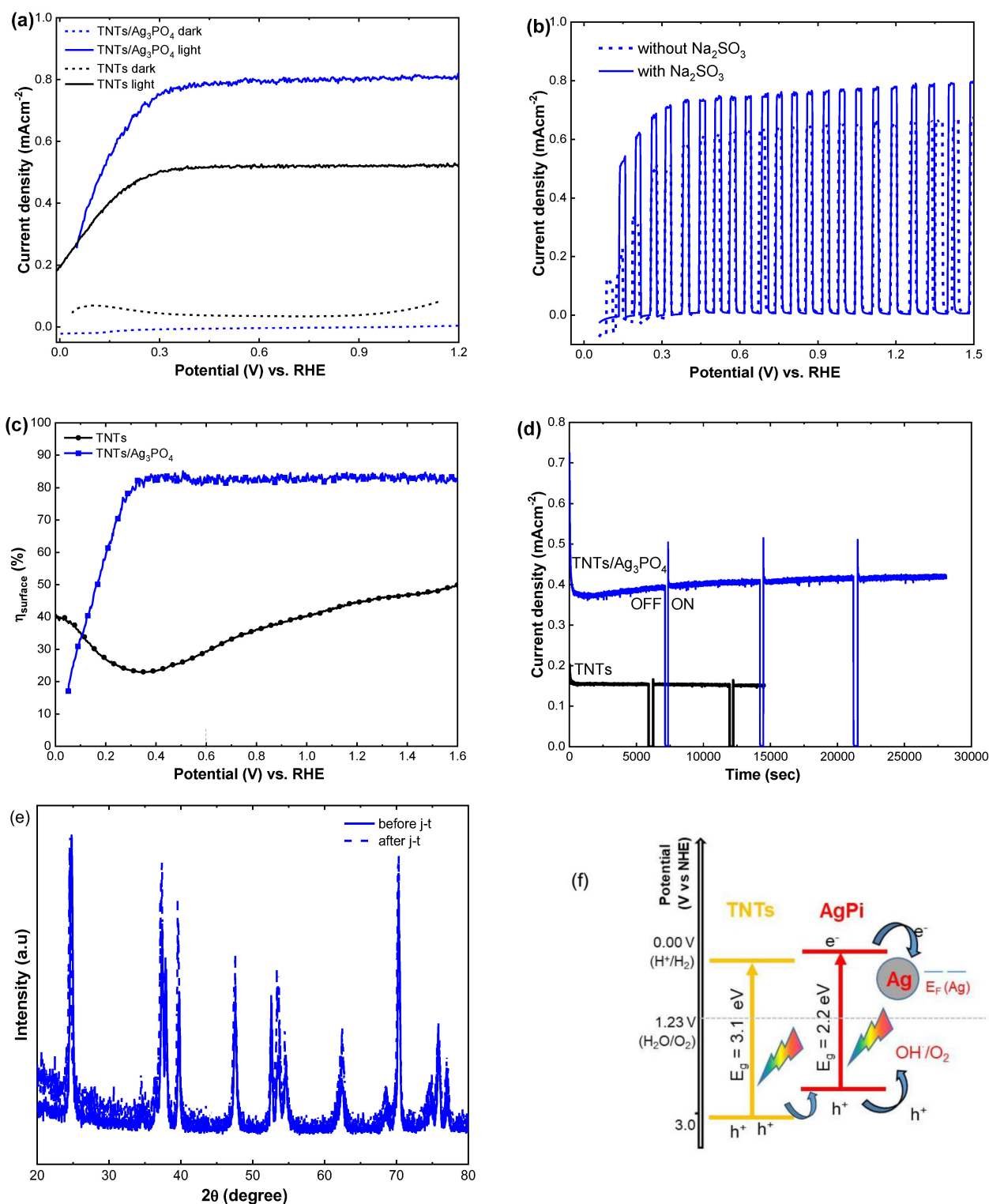


Figure 7. (a) Linear sweep voltammogram plots of TNTs (black) and TNTs/Ag₃PO₄ (blue) under continuous illuminations in 0.1 M PBS and 1 M Na₂SO₃ as hole scavenger and chopped (b) illumination of TNTs/Ag₃PO₄ photoanodes with and without 1 M Na₂SO₃; (c) plots of η_{surface} vs. applied bias acquired for bare TNTs and composite TNTs/Ag₃PO₄ films; (d) chronoamperometric measurements at 1.23 V_{RHE} of the long-lasting photostability of the TNTs and TNTs/Ag₃PO₄ array films evaluated in 0.1 M PBS (pH 7.5) under continuous irradiations (AM 1.5 G). (e) X-ray diffraction patterns of TNTs/Ag₃PO₄ array films earlier (solid) and after (dashed) 8 h of the chronoamperometric test (f) mechanistic illustration of TNTs/Ag₃PO₄ array film.

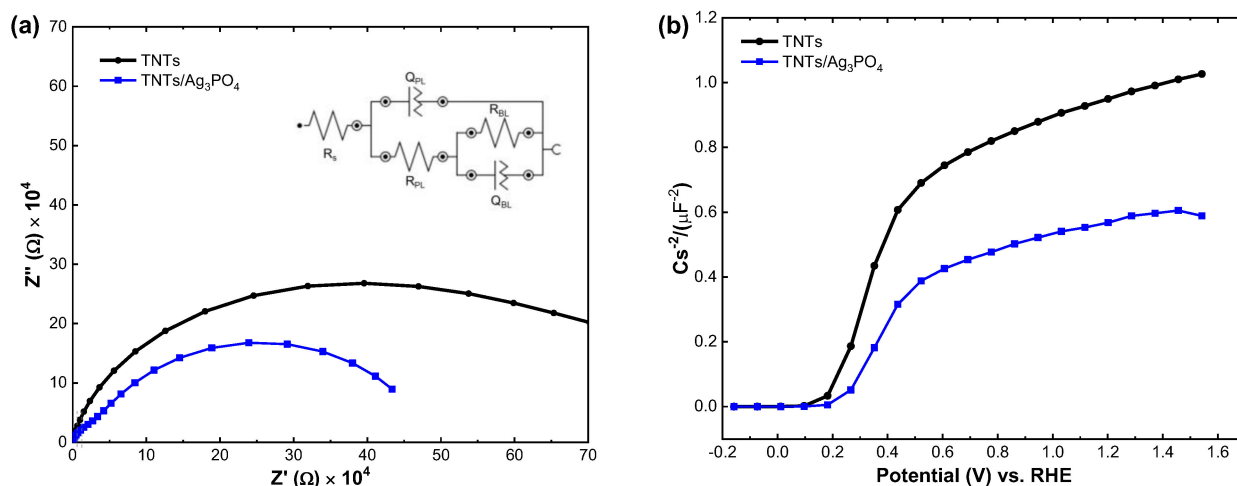


Figure 8. (a) Nyquist plots of fabricated TNTs array films and photodeposited Ag₃PO₄ over the surface of TNTs (TNTs/Ag₃PO₄) composite array films. The measurements were executed at 1.0 V_{RHE}, at frequencies varying from 100 kHz to 0.05 Hz, and the inset shows the equivalent circuit. (b) Mott–Schottky measurements for unmodified TNTs, and TNTs/Ag₃PO₄ electrodes under the dark condition at 100 Hz.

To further gain insight into the effect of Ag₃PO₄ on the electrical performances of TNTs, the Mott–Schottky curves of the fabricated array films are displayed in Figure 8b. Interestingly, the obtained Mott–Schottky plots of the pure TNTs and the composite TNTs/Ag₃PO₄ array films revealed a positive slope, as expected for n-type semiconductor electrodes. Obviously, the acquired curves remarkably validated that the fabricated composite array films had a lesser slope than their pure TNTs, indicating the enriched carrier density and also the improve conductivity features of the former [53]. In particular, the assessed carrier density of the fabricated TNTs/Ag₃PO₄ was $2.8 \times 10^{19} \text{ cm}^{-3}$, greater than that of the pure TNTs electrodes ($7.90 \times 10^{18} \text{ cm}^{-3}$). The higher carrier density can be credited first to defect doping in the TNTs bulk, which is responsible for the reduction of the bandgap observed above. In addition, the decoration of the lower bandgap Ag₃PO₄ will result in a higher effective carrier density of the composite film. Furthermore, as seen in Figure 8b, by assuming the M–S curves to the potential axis, the flat band potentials (E_{FB}) of the pure TNTs and their composite TNTs/Ag₃PO₄ array films were assessed to be 0.048 and 0.19 V vs. RHE, respectively. Moreover, the E_{FB} of the composite TNTs/Ag₃PO₄ array films was effectively moved positively and inferior to its parent TNTs, agreeing with the electrochemical variations of the overpotential oxygen evolution reaction. In the case of the TNTs/Ag₃PO₄ array films, the obvious positive shift of E_{FB} enhanced the band bending at the composite TNTs/Ag₃PO₄ array films and electrolyte interface, thereby decreasing the recombination of the photoinduced electron-hole pairs and their overpotential in the oxygen evolution reaction kinetics of the TNTs/Ag₃PO₄ composite array films.

3. Experimental Section

3.1. Chemicals

Ti foils (>99.5%, Alfa Aesar, Kandel, Germany) were applied to synthesize TNTs. Ammonium fluoride (NH₄F) and (Sigma Aldrich, St. Louis, MI, USA), silver nitrate, and sodium sulfite (Na₂SO₃) were received from Sigma Aldrich (St. Louis, MI, USA). Sodium phosphate (NaH₂PO₄, ≥99.0% and Na₂HPO₄, ≥98.0%, Sigma Aldrich, St. Louis, MI, USA) was applied to fabricate the phosphate buffer solution (PBS). Ethylene glycol (EG) was received from BDH.

3.2. Fabrication of TNTs/Ag₃PO₄ Photoanodes

TNTs films were synthesized through a dual-step anodization method of Ti substrates under normal circumstances, as previously reported [32]. A series of silver nanoparticles were decorated over the surface of TNTs photoanodes via a chemical photodeposition process. Subsequently, the incorporation of Ag nanoparticles over TNTs films was implemented by impregnating the array of films in a AgNO₃ solution for 5 min. Afterward, the obtained electrodes were taken out and then cleaned with water and dried out in an N₂ atmosphere. Later, the subsequent electrode films were kept under the UV lamp (400 W) for 60 min and then cleaned with water and dried out in the air. Similarly, a series of Ag nanoparticles and an AgNO₃ solution with altered concentrations were exploited, and the AgNO₃ concentration tuned from 0.025 to 0.2 M. The obtained electrode is labeled as TNTs/Ag. In order to acquire the Ag₃PO₄ nanoparticles, the obtained films were subjected to cyclic voltammetric scans within the range of −0.5 to 1.6 V (vs Ag/AgCl) in a PBS (0.1 M, pH 7.5), at the scan rate of 50 mV/s. Figure S1 demonstrates the different steps of the synthetic process involved in developing the TNTs/Ag₃PO₄ electrode materials.

3.3. Materials Characterization

The morphological features of the photoanodes were examined via field effect SEM (FE-SEM; JEOL JSM-7000F, Tokyo, Japan). Diffuse reflectance UV-Vis spectra were evaluated in a Shimadzu UV-3600 spectrophotometer. The crystal features of fabricated electrodes were studied by the Rigaku XtaLAB Mini II benchtop system. The surface features of the electrode materials were examined through an X-ray Photoelectron Spectrometer (JEOL JPS-9030, Tokyo, Japan). PEC measurements were carried out through an electrochemical system (PGSTAT30) below AM 1.5G solar irradiation. All the PEC analyses were evaluated in a 0.1 M PBS.

The applied bias photon-to-current efficiency (ABPE) of the fabricated materials was assessed through the linear sweep voltammogram (LSV) plots obtained in Equation (1).

$$ABPE (\%) = \frac{J_{PEC} (\text{mA}/\text{cm}^2) \times (1.23 - V_{bias})V}{P_{in} (\text{mW}/\text{cm}^2)} \times 100 \quad (1)$$

where J_{PEC} is the photocurrent density, V_{bias} is the applied potential, and P_{in} is the incident irradiation power density.

The surface charge transfer efficiency of the electrodes was obtained using Equation (2).

$$\eta_{\text{surface}} = \frac{J_{H_2O}}{J_{Na_2SO_3}} \times 100 \quad (2)$$

where J_{H_2O} and $J_{Na_2SO_3}$ are the photocurrents measured in the 0.1 M PBS without and with 1 M Na₂SO₃, respectively.

4. Conclusions

In summary, heterostructured Ag₃PO₄/TNTs electrodes were fabricated by a facile anodic oxidation method and chemical photodeposition process. Well-aligned TNTs were fabricated, and their decoration by Ag₃PO₄ essentially did not alter the homogeneity and tubular structure of the film as revealed by FESEM and HRTEM. The TNTs/Ag₃PO₄ composite presented a remarkable photocurrent density of 0.74 mA/cm² at 1.23 V versus RHE, compared to 0.25 mA/cm² for the undecorated TNT film, with a remarkably reduced on-set potential. In addition, the charge transfer efficiency was calculated to be 84% (compared to <35% for the pure electrode), with enhanced durability with only a 35% photocurrent loss after 8 h of operation. Also, the onset potential of the TNTs/Ag₃PO₄ array films declined to 0.06 V_{RHE}, and the ABPE was 0.53%. The EIS examination validated that the synthesized Ag₃PO₄ layer provided efficient charge transfer kinetics and reduced electron-hole recombination. These observed outcomes show this to be an effective tactic

for designing new kinds of photoelectrode materials based on rare-earth materials for PEC and photocatalytic uses.

Supplementary Materials: The following supporting information can be downloaded at: <https://www.mdpi.com/article/10.3390/catal12111440/s1>, Figure S1. Schematic representation of fabrication process; Figure S2. FESEM analysis of the fabricated electrodes after durability test; Table S1. comparison table with literature; Table S2. Impedance parameter values derived from the fitting to the equivalent circuit for the impedance spectra were examined under constant illumination conditions at 1.0 V vs. RHE. References [20,28,53–63] are cited in Supplementary Materials.

Author Contributions: Conceptualization, P.A.; methodology, H.A.A.; investigation, P.A., M.S.A. and M.H.; formal analysis, P.A., M.S.A. and H.A.A., data curation, P.A., M.S.A. and H.A.A.; writing—original draft preparation, P.A., supervision, M.A.-S. and A.M.A.-M., project administration, A.M.A.-M. All authors have read and agreed to the published version of the manuscript.

Funding: This project was funded by the National Plan for Science, Technology, and Innovation (MAARIFAH), King Abdulaziz City for Science and Technology, Saudi Arabia, grant number (3-17-02-001-0011).

Data Availability Statement: All data generated or analyzed during this study are included in this published article (and its Supplementary Materials).

Acknowledgments: This project was funded by the National Plan for Science, Technology, and Innovation (MAARIFAH), King Abdulaziz City for Science and Technology, Saudi Arabia, Award Number (3-17-02-001-0011).

Conflicts of Interest: The authors declare no conflict of interest.

References

1. Wang, S.; Liu, G.; Wang, L. Crystal facet engineering of photoelectrodes for photoelectrochemical water splitting. *Chem. Rev.* **2019**, *119*, 5192–5247. [[CrossRef](#)] [[PubMed](#)]
2. Tran-Phu, T.; Fusco, Z.; Di Bernardo, I.; Lipton-Duffin, J.; Toe, C.Y.; Daiyan, R.; Tricoli, A. Understanding the role of vanadium vacancies in BiVO₄ for efficient photoelectrochemical water oxidation. *Chem. Mater.* **2021**, *33*, 3553–3565. [[CrossRef](#)]
3. Yao, T.; An, X.; Han, H.; Chen, J.Q.; Li, C. Photoelectrocatalytic materials for solar water splitting. *Adv. Energy Mater.* **2018**, *8*, 1800210. [[CrossRef](#)]
4. Rosman, N.N.; Yunus, R.M.; Shah, N.R.A.M.; Shah, R.M.; Arifin, K.; Minggu, L.J.; Ludin, N.A. An overview of co-catalysts on metal oxides for photocatalytic water splitting. *Int. J. Energy Res.* **2022**, *46*, 11596–11619. [[CrossRef](#)]
5. Liu, Z.; Xu, K.; Yu, H.; Sun, Z. Synergistic effect of Ag/MoS₂/TiO₂ heterostructure arrays on enhancement of photoelectrochemical and photocatalytic performance. *Int. J. Energy Res.* **2021**, *45*, 6850–6862. [[CrossRef](#)]
6. Feng, W.; Lin, L.; Li, H.; Chi, B.; Pu, J.; Li, J. Hydrogenated TiO₂/ZnO heterojunction nanorod arrays with enhanced performance for photoelectrochemical water splitting. *Int. J. Hydrog. Energy* **2017**, *42*, 3938–3946. [[CrossRef](#)]
7. Kawasaki, S.; Nakatsuji, K.; Yoshinobu, J.; Komori, F.; Takahashi, R.; Lippmaa, M.; Kudo, A. Epitaxial Rh-doped SrTiO₃ thin film photocathode for water splitting under visible light irradiation. *Appl. Phys. Lett.* **2012**, *101*, 033910. [[CrossRef](#)]
8. Sharma, P.; Jang, J.W.; Lee, J.S. Key strategies to advance the photoelectrochemical water splitting performance of α -Fe₂O₃ photoanode. *ChemCatChem* **2019**, *11*, 157–179. [[CrossRef](#)]
9. Yu, S.Q.; Ling, Y.H.; Zhang, J.; Qin, F.; Zhang, Z.J. Efficient photoelectrochemical water splitting and impedance analysis of WO₃-x nanoflake electrodes. *Int. J. Hydrog. Energy* **2017**, *42*, 20879–20887. [[CrossRef](#)]
10. Amer, M.S.; Arunachalam, P.; Al-Mayouf, A.M.; Prasad, S.; Alshalwi, M.N.; Ghanem, M.A. Mesoporous tungsten trioxide photoanodes modified with nitrogen-doped carbon quantum dots for enhanced oxygen evolution photo-reaction. *Nanomaterials* **2019**, *9*, 1502. [[CrossRef](#)]
11. Soundarya, T.L.; Jayalakshmi, T.; Alsaiani, M.A.; Jalalah, M.; Abate, A.; Alharthi, F.A.; Nagaraju, G. Ionic Liquid-Aided Synthesis of Anatase TiO₂ Nanoparticles: Photocatalytic Water Splitting and Electrochemical Applications. *Crystals* **2022**, *12*, 1133. [[CrossRef](#)]
12. Liu, M.; de Leon Snapp, N.; Park, H. Water photolysis with a cross-linked titanium dioxide nanowire anode. *Chem. Sci.* **2011**, *2*, 80–87. [[CrossRef](#)]
13. Tang, H.; Prasad, K.; Sanjines, R.; Schmid, P.E.; Levy, F. Electrical and optical properties of TiO₂ anatase thin films. *J. Appl. Phys.* **1994**, *75*, 2042–2047. [[CrossRef](#)]
14. Serga, V.; Burve, R.; Krumina, A.; Romanova, M.; Kotomin, E.A.; Popov, A.I. Extraction-pyrolytic method for TiO₂ polymorphs production. *Crystals* **2021**, *11*, 431. [[CrossRef](#)]
15. Hoyer, P. Semiconductor nanotube formation by a two-step template process. *Adv. Mater.* **1996**, *8*, 857–859. [[CrossRef](#)]
16. Rempel, A.A.; Valeeva, A.A.; Vokhmintsev, A.S.; Weinstein, I.A. Titanium dioxide nanotubes: Synthesis, structure, properties and applications. *Russ. Chem. Rev.* **2021**, *90*, 1397. [[CrossRef](#)]

17. Wang, J.; Lin, Z. Dye-sensitized TiO₂ nanotube solar cells with markedly enhanced performance via rational surface engineering. *Chem. Mater.* **2010**, *22*, 579–584. [[CrossRef](#)]
18. Qin, P.; Paulose, M.; Dar, M.I.; Moehl, T.; Arora, N.; Gao, P.; Varghese, O.K.; Grätzel, M.; Nazeeruddin, M.K. Stable and efficient perovskite solar cells based on titania nanotube arrays. *Small* **2015**, *11*, 5533–5539. [[CrossRef](#)]
19. Macak, J.M.; Tsuchiya, H.; Ghicov, A.; Yasuda, K.; Hahn, R.; Bauer, S.; Schmuki, P. TiO₂ nanotubes: Self-organized electrochemical formation, properties and applications. *Curr. Opin. Solid State Mater. Sci.* **2007**, *11*, 3–18. [[CrossRef](#)]
20. Arunachalam, P.; AlOraij, H.A.; Amer, M.S.; Hezam, M.; Shaddad, M.N.; Madhavan, J. Activation effect of nickel phosphate co-catalysts on the photoelectrochemical water oxidation performance of TiO₂ nanotubes. *J. Saudi Chem. Soc.* **2022**, *26*, 101484. [[CrossRef](#)]
21. Sang, Y.; Zhao, Z.; Tian, J.; Hao, P.; Jiang, H.; Liu, H.; Claverie, J.P. Enhanced photocatalytic property of reduced graphene oxide/TiO₂ nanobelt surface heterostructures constructed by an in situ photochemical reduction method. *Small* **2014**, *10*, 3775–3782. [[CrossRef](#)]
22. Chen, X.; Shen, S.; Guo, L.; Mao, S.S. Semiconductor-based photocatalytic hydrogen generation. *Chem. Rev.* **2010**, *110*, 6503–6570. [[CrossRef](#)] [[PubMed](#)]
23. Lee, M.H.; Park, J.H.; Han, H.S.; Song, H.J.; Cho, I.S.; Noh, J.H.; Hong, K.S. Nanostructured Ti-doped hematite (α -Fe₂O₃) photoanodes for efficient photoelectrochemical water oxidation. *Int. J. Hydrogen Energy* **2014**, *39*, 17501–17507. [[CrossRef](#)]
24. Murphy, A.B.; Barnes, P.R.F.; Randeniya, L.K.; Plumb, I.C.; Grey, I.E.; Horne, M.D.; Glasscock, J.A. Efficiency of solar water splitting using semiconductor electrodes. *Int. J. Hydrogen Energy* **2006**, *31*, 1999–2017. [[CrossRef](#)]
25. Liu, Q.; Ding, D.; Ning, C.; Wang, X. Cobalt-phosphate/Ni-doped TiO₂ nanotubes composite photoanodes for solar water oxidation. *Mater. Sci. Eng. B* **2015**, *202*, 54–60. [[CrossRef](#)]
26. Li, X.; Elshahawy, A.M.; Guan, C.; Wang, J. Metal phosphides and phosphates-based electrodes for electrochemical supercapacitors. *Small* **2017**, *13*, 1701530. [[CrossRef](#)]
27. Cao, S.; Wang, C.J.; Fu, W.F.; Chen, Y. Metal phosphides as co-catalysts for photocatalytic and photoelectrocatalytic water splitting. *ChemSusChem* **2017**, *10*, 4306–4323. [[CrossRef](#)]
28. Ai, G.; Mo, R.; Li, H.; Zhong, J. Cobalt phosphate modified TiO₂ nanowire arrays as co-catalysts for solar water splitting. *Nanoscale* **2015**, *7*, 6722–6728. [[CrossRef](#)]
29. Wen, P.; Su, F.; Li, H.; Sun, Y.; Liang, Z.; Liang, W.; Jiang, L. A Ni₂P nanocrystal cocatalyst enhanced TiO₂ photoanode towards highly efficient photoelectrochemical water splitting. *Chem. Eng. J.* **2020**, *385*, 123878. [[CrossRef](#)]
30. Huang, G.-F.; Ma, Z.-L.; Huang, W.-Q.; Tian, Y.; Jiao, C.; Yang, Z.-M.; Wan, Z.; Pan, A. Semiconductor Photocatalyst: Possibilities and Challenges. *J. Nanomater.* **2013**, *2013*, 1.
31. Pan, J.; Liu, G. Facet Control of Photocatalysts for Water Splitting. In *Semiconductors and Semimetals*; Mi, Z., Wang, L., Jagadish, C., Eds.; Elsevier: Amsterdam, The Netherlands, 2017; Chapter 10; Volume 97, pp. 349–391.
32. Shaddad, M.N.; Cardenas-Morcoso, D.; Arunachalam, P.; García-Tecedor, M.; Ghanem, M.A.; Bisquert, J.; Gimenez, S. Enhancing the optical absorption and interfacial properties of BiVO₄ with Ag₃PO₄ nanoparticles for efficient water splitting. *J. Phys. Chem. C* **2018**, *122*, 11608–11615. [[CrossRef](#)]
33. Raj, A.K.; Murugan, C.; Pandikumar, A. Efficient photoelectrochemical reduction of carbon dioxide into alcohols assisted by photoanode driven water oxidation with gold nanoparticles decorated titania nanotubes. *J. CO₂ Util.* **2021**, *52*, 101684.
34. Fadlallah, M.M.; Eckern, U. Electronic and optical properties of metal-doped TiO₂ nanotubes: Spintronic and photocatalytic applications. *New J. Phys.* **2020**, *22*, 093028. [[CrossRef](#)]
35. Shaddad, M.N.; Cardenas-Morcoso, D.; García-Tecedor, M.; Fabregat-Santiago, F.; Bisquert, J.; Al-Mayouf, A.M.; Gimenez, S. TiO₂ nanotubes for solar water splitting: Vacuum annealing and Zr doping enhance water oxidation kinetics. *ACS Omega* **2019**, *4*, 16095–16102. [[CrossRef](#)] [[PubMed](#)]
36. Mohamed, I.M.; Dao, V.D.; Yasin, A.S.; Barakat, N.A.; Choi, H.S. Design of an efficient photoanode for dye-sensitized solar cells using electrospun one-dimensional GO/N-doped nanocomposite SnO₂/TiO₂. *Appl. Surf. Sci.* **2017**, *400*, 355–364. [[CrossRef](#)]
37. Patterson, A.L. The Scherrer formula for X-ray particle size determination. *Phys. Rev.* **1939**, *56*, 978. [[CrossRef](#)]
38. Langford, J.I.; Wilson, A.J.C. Scherrer after sixty years: A survey and some new results in the determination of crystallite size. *J. Appl. Crystallogr.* **1978**, *11*, 102–113. [[CrossRef](#)]
39. Lele, S.; Anantharaman, T.R. Influence of crystallite shape on particle size broadening of Debye-Scherrer reflections. In *Proceedings of the Indian Academy of Sciences-Section A*; Springer: Delhi, India, 1966; Volume 64, pp. 261–274.
40. Kernazhitsky, L.; Shymanovska, V.; Gavrilko, T.; Naumov, V.; Fedorenko, L.; Kshnyakin, V.; Baran, J. Photoluminescence of Cr-doped TiO₂ induced by intense UV laser excitation. *J. Lumin.* **2015**, *166*, 253–258. [[CrossRef](#)]
41. Xu, M.; Da, P.; Wu, H.; Zhao, D.; Zheng, G. Controlled Sn-doping in TiO₂ nanowire photoanodes with enhanced photoelectrochemical conversion. *Nano Lett.* **2012**, *12*, 1503–1508. [[CrossRef](#)]
42. Teng, W.; Li, X.; Zhao, Q.; Chen, G. Fabrication of Ag/Ag₃PO₄/TiO₂ Heterostructure Photoelectrodes for Efficient Decomposition of 2-Chlorophenol under Visible Light Irradiation. *J. Mater. Chem. A* **2013**, *1*, 9060–9068. [[CrossRef](#)]
43. Mohamed, I.M.; Dao, V.D.; Yasin, A.S.; Mousa, H.M.; Mohamed, H.O.; Choi, H.S.; Barakat, N.A. Nitrogen-doped SnO₂-incorporated TiO₂ nanofibers as novel and effective photoanode for enhanced efficiency dye-sensitized solar cells. *Chem. Eng. J.* **2016**, *304*, 48–60.

44. Randeniya, L.K.; Bendavid, A.; Martin, P.J.; Preston, E.W. Photoelectrochemical and structural properties of TiO₂ and N-doped TiO₂ thin films synthesized using pulsed direct current plasma-activated chemical vapor deposition. *J. Phys. Chem. C* **2007**, *111*, 18334–18340. [[CrossRef](#)]
45. Chen, F.; Yang, Q.; Li, X.; Zeng, G.; Wang, D.; Niu, C.; Zhao, J.; An, H.; Xie, T.; Deng, Y. Hierarchical Assembly of Graphene-Bridged Ag₃PO₄/Ag/BiVO₄ (040) Z-Scheme Photocatalyst: An Efficient, Sustainable and Heterogeneous Catalyst with Enhanced Visible-Light Photoactivity towards Tetracycline Degradation under Visible Light Irradiation. *Appl. Catal. B* **2017**, *200*, 330–342. [[CrossRef](#)]
46. Teng, W.; Li, X.; Zhao, Q.; Zhao, J.; Zhang, D. In Situ Capture of Active Species and Oxidation Mechanism of Rhb and Mb Dyes over Sunlight-Driven Ag/Ag₃PO₄ Plasmonic Nanocatalyst. *Appl. Catal. B* **2012**, *125*, 538–545. [[CrossRef](#)]
47. Feng, D.; Luo, W.; Zhang, J.; Xu, M.; Zhang, R.; Wu, H.; Zhao, D. Multi-layered mesoporous TiO₂ thin films with large pores and highly crystalline frameworks for efficient photoelectrochemical conversion. *J. Mater. Chem. A* **2013**, *1*, 1591–1599. [[CrossRef](#)]
48. Haro, M.; Abargues, R.; Herraiz-Cardona, I.; Martínez-Pastor, J.; Giménez, S. Plasmonic versus catalytic effect of gold nanoparticles on mesoporous TiO₂ electrodes for water splitting. *Electrochim Acta* **2014**, *144*, 64–70. [[CrossRef](#)]
49. He, Y.; Zhu, J.; Yuan, Y.; Li, M.; Yang, Y.; Liu, Y.; Chen, M.; Cao, D.; Yan, X. Dual-Regulation Charge Separation Strategy with the Synergistic Effect of 1D/0D Heterostructure and Inserted Ferro-electric Layer for Boosting Photoelectrochemical Water Oxidation. *J. Mater. Chem. A* **2021**, *9*, 7594–7605. [[CrossRef](#)]
50. Ye, S.; Ding, C.; Chen, R.; Fan, F.; Fu, P.; Yin, H.; Li, C. Mimicking the key functions of photosystem II in artificial photosynthesis for photoelectrocatalytic water splitting. *J. Am. Chem. Soc.* **2018**, *140*, 3250–3256. [[CrossRef](#)]
51. Abd El-Lateef, H.M.; Khalaf, M.M.; Dao, V.D.; Mohamed, I.M. Electrochemical Impedance Investigation of Dye-Sensitized Solar Cells Based on Electrospun TiO₂ Nanofibers Photoanodes. *Materials* **2022**, *15*, 6175. [[CrossRef](#)]
52. Bredar, A.R.; Chown, A.L.; Burton, A.R.; Farnum, B.H. Electrochemical impedance spectroscopy of metal oxide electrodes for energy applications. *ACS Appl. Energy Mater.* **2020**, *3*, 66–98. [[CrossRef](#)]
53. Shaddad, M.N.; Arunachalam, P.; Amer, M.S.; Al-Mayouf, A.M.; Hezam, M.; AlOrajib, H.A.; Gimenez, S. Exploiting the synergistic catalytic effects of CoPi nanostructures on Zr-doped highly ordered TiO₂ nanotubes for efficient solar water oxidation. *Int. J. Energy Res.* **2022**, *46*, 12608–12622. [[CrossRef](#)]
54. Hoang, S.; Guo, S.; Hahn, N.T.; Bard, A.J.; Mullins, C.B. Visible Light Driven Photoelectrochemical Water Oxidation on Nitrogen-Modified TiO₂ Nanowires. *Nano Lett.* **2012**, *12*, 26–32. [[CrossRef](#)] [[PubMed](#)]
55. Ai, G.; Li, H.; Liu, S.; Mo, R.; Zhong, J. Solar Water Splitting by TiO₂/CdS/Co–Pi Nanowire Array Photoanode Enhanced with Co–Pi as Hole Transfer Relay and CdS as Light Absorber. *Adv. Funct. Mat.* **2015**, *25*, 5706–5713. [[CrossRef](#)]
56. Liu, D.; Jing, L.; Luan, P.; Tang, J.; Fu, H. Enhancement effects of cobalt phosphate modification on activity for photoelectrochemical water oxidation of TiO₂ and mechanism insights. *ACS Appl. Mater. Interfaces* **2013**, *5*, 4046–4052. [[CrossRef](#)] [[PubMed](#)]
57. Xu, Y.; Ahmed, R.; Lin, Q.; Zangari, G. (Photo) electrochemical water oxidation at anodic TiO₂ nanotubes modified by electrodeposited NiFe oxy-hydroxides catalysts. *Electrochim. Acta* **2019**, *308*, 91–98. [[CrossRef](#)]
58. Momeni, M.M.; Ghayeb, Y.; Davarzadeh, M. Single-step electrochemical anodization for synthesis of hierarchical WO₃–TiO₂ nanotube arrays on titanium foil as a good photoanode for water splitting with visible light. *J. Electroanal. Chem.* **2015**, *739*, 149–155. [[CrossRef](#)]
59. Xu, C.; Song, Y.; Lu, L.; Cheng, C.; Liu, D.; Fang, X.; Chen, X.; Zhu, X.; Li, D. Electrochemically hydrogenated TiO₂ nanotubes with improved photoelectrochemical water splitting performance. *Nanoscale Res Lett* **2013**, *8*, 1–7. [[CrossRef](#)]
60. Liu, C.; Zhang, C.; Yin, G.; Zhang, T.; Wang, W.; Ou, G.; Jin, H.; Chen, Z. A Three-Dimensional Branched TiO₂ Photoanode with an Ultrathin Al₂O₃ Passivation Layer and a NiOOH Cocatalyst toward Photoelectrochemical Water Oxidation. *ACS Appl. Mater. Interfaces* **2021**, *13*, 13301–13310. [[CrossRef](#)]
61. Kang, Q.; Cao, J.; Zhang, Y.; Liu, L.; Xu, H.; Ye, J. Reduced TiO₂ nanotube arrays for photoelectrochemical water splitting. *J. Mater. Chem. A* **2013**, *1*, 5766–5774. [[CrossRef](#)]
62. Altomare, M.; Lee, K.; Killian, M.S.; Selli, E.; Schmuki, P. Ta-Doped TiO₂ Nanotubes for Enhanced Solar-Light Photoelectrochemical Water Splitting. *Eur. J. Chem.* **2013**, *19*, 5841–5844. [[CrossRef](#)]
63. Shaddad, M.N.; Ghanem, M.A.; Al-Mayouf, A.M.; Gimenez, S.; Bisquert, J.; Herraiz-Cardona, I. Cooperative Catalytic Effect of ZrO₂ and α-Fe₂O₃ Nanoparticles on BiVO₄ Photoanodes for Enhanced Photoelectrochemical Water Splitting. *ChemSusChem* **2016**, *9*, 2779–2783. [[CrossRef](#)]